JOURNAL OF GEOPHYSICAL RESEARCH, VOL. 112, F03020, doi:10.1029/2006JF000724, 2007

A full-stress, thermomechanical flow band model using the finite volume method

S. F. Price,[1,2] E. D. Waddington,[1] and H. Conway[1]

Received 16 November 2006; revised 3 April 2007; accepted 25 May 2007; published 21 August 2007.

[1] A thermomechanical ice flow model is formulated using the finite volume method. Separate submodels solve the full, two-dimensional momentum equations, the advective-diffusive heat equation, and evolution of the free surface. A unique aspect of the method is the use of a boundary-fitted, orthogonal, curvilinear coordinate system, which simplifies the implementation of boundary conditions, leads to a straightforward discretization scheme, and results in banded sparse coefficient matrices that can be inverted directly. For simple boundary conditions and geometries, the model compares well with analytical solutions. For more complicated boundary conditions and geometries, the model compares well with full-stress solutions obtained by previous authors.

Citation: Price, S. F., E. D. Waddington, and H. Conway (2007), A full-stress, thermomechanical flow band model using the finite volume method, *J. Geophys. Res.*, *112*, F03020, doi:10.1029/2006JF000724.

1. Introduction

[2] When modeling the flow of large ice masses, a number of simplifications are often employed. The most common of these is the "shallow-ice" approximation in which horizontal stress gradients are ignored under the assumption that the ice thickness H is small compared to its lateral extent [e.g., *Fowler and Larson*, 1978; *Hutter*, 1981]. This approximation is valid for portions of the ice sheet that deform primarily through simple shear but not for regions of transitional flow, where additional components of the stress tensor are important. Longitudinal stress gradients are particularly important near ice divides [*Raymond*, 1983], in regions where basal relief varies significantly over distances of order H [*Budd*, 1970a, 1970b; *Whillans and Johnsen*, 1983], and in regions of flow transition such as the tributaries to ice streams [*Price et al.*, 2002].

[3] Finite difference (FDM) and finite element (FEM) methods have been used successfully to construct full-stress and "higher-order" flow models that account for horizontal stress gradients in ice flow [e.g., *Raymond*, 1983; *Hvidberg*, 1996; *Pattyn*, 2002a]. The finite volume method (FVM) or "control volume method" [*Patankar*, 1980; *Versteeg and Malalasekera*, 1995] is another method for solving the full-stress equations without resorting to higher-order approximations. Here, we formulate a new thermomechanical flow band model in orthogonal, curvilinear coordinates using the FVM. To our knowledge, the method has not been previously applied to ice flow. First we present and discuss the governing equations, the coordinate system, and the solution method. We then test the model by comparing results for simple domain geometries and boundary conditions against analytical solutions, and by comparing results for more complex conditions with results published by others. In other studies we have used our model to investigate the flow and thickness history of Siple Dome, an interstream ridge in West Antarctica [*Price et al.*, 2007], to investigate the potential for inland migration of ice streams [*Price et al.*, 2005], and to model the evolution of a glacier being deformed by an expanding lava dome [*Price and Walder*, 2007].

2. Governing Equations

2.1. Conservation of Momentum

[4] In Cartesian coordinates with the x axis oriented along flow, the y axis oriented across flow, and the z axis vertical and perpendicular to the x, y plane, conservation of momentum along the x_i direction requires

$$\frac{\partial(\rho u_i)}{\partial t} + u_j \frac{\partial(\rho u_i)}{\partial x_j} = \frac{\partial}{\partial x_j}\left(\eta \frac{\partial u_i}{\partial x_j}\right) - \frac{\partial P}{\partial x_i} + \rho g_i \qquad (i = x, y, z). \tag{1}$$

[5] Summation over repeat indices is implied here (and in the remainder of the paper); u_i are the components of the velocity vector in the coordinate directions x, y, and z. P is the mean compressive stress, ρ is the ice density, η is the effective viscosity, and g is the gravitational acceleration. For ice flow, accelerations are negligible and the Reynolds number is on the order of $\sim 10^{-16}$. In this case, the nonsteady and advective terms on the left-hand side of equation (1) $\rightarrow 0$ giving

$$\frac{\partial}{\partial x_j}\left(\eta \frac{\partial u_i}{\partial x_j}\right) - \frac{\partial P}{\partial x_i} + \rho g_i = 0 \qquad (i = x, y, z). \tag{2}$$

[1]Department of Earth and Space Sciences, University of Washington, Seattle, Washington, USA.
[2]Now at Bristol Glaciology Centre, School of Geographical Sciences, University of Bristol, Bristol, UK.

0148-0227/07/2006JF000724$09.00

Table 1. Constants and Other Model Parameters

Symbol	Constant	Value	Units
A_0	flow law constant ($\theta > 263$ K)	6.26[a]	10^{10} Pa^{-3} a^{-1}
A_0	flow law constant ($\theta \leq 263$ K)	1.3[a]	10^{5} Pa^{-3} a^{-1}
C	specific heat	$C(\theta) = 152.5 + 7.12\cdot\theta$[b]	J kg^{-1} K^{-1}
g	gravitational acceleration	9.81	m s^{-2}
k	conductivity	$k(\theta) = 9.828\cdot\exp(-0.0057\cdot\theta)$[b]	W K^{-1} m^{-1}
L	characteristic length scale	1015	m
n	power law exponent	3	–
Q	activation energy ($\theta > 263$ K)	139[a]	10^{3} J mol^{-1}
Q	activation energy ($\theta \leq 263$ K)	60[a]	10^{3} J mol^{-1}
Q_{geo}	geothermal flux	70[c]	10^{-3} W m^{-2}
R	universal gas constant	8.314	J mol^{-1} K^{-1}
ρ	density of ice	918	kg m^{-3}

[a]See *Paterson* [1994, pp. 86, 97].
[b]See *Paterson* [1994, p. 205].
[c]See *Engelhardt* [2004] and G. Clow (personal communication, 2005).

[6] Ice is assumed to be incompressible:

$$\frac{\partial u_i}{\partial x_i} = 0. \tag{3}$$

[7] For flow in plane strain (i.e., gradients in the y direction are negligible), the along-flow (u) and the vertical (w) components of the velocity, together with the incompressibility condition, are used to solve for the horizontal and vertical velocity fields and the pressure field. Details of the solution procedure are discussed below.

2.2. Conservation of Energy

[8] Conservation of energy requires that nonsteady and advective changes in temperature are balanced by diffusive heat flux and internal sources:

$$\frac{\partial \theta}{\partial t} + u_i \frac{\partial \theta}{\partial x_i} = \frac{1}{\rho C}\frac{\partial}{\partial x_i}\left(k\frac{\partial \theta}{\partial x_i}\right) + \frac{\sigma_{ij}\dot{\varepsilon}_{ij}}{\rho C}, \tag{4}$$

where θ is the absolute ice temperature. Although the specific heat capacity C and the thermal conductivity k are temperature-dependent, for simplicity we do not specify the dependence when writing out the equation. We assume that ice density is constant, and that liquid water is not present in the ice even at the pressure melting point.

2.3. Constitutive Relation

[9] We use a generalized form of Glen's flow law [*Nye*, 1957]:

$$\tau_{ij} = B(\theta)\dot{\varepsilon}_e^{\frac{1-n}{n}}\dot{\varepsilon}_{ij}, \tag{5}$$

where τ_{ij} is the deviatoric stress tensor, $\dot{\varepsilon}_{ij}$ is the strain rate tensor, and $B(\theta) = A(\theta)^{\frac{-1}{n}}$ is the inverse rate factor. The rate factor follows an Arrhenius relation: $A(\theta) = A_0 \exp(-Q/R\theta)$; values of A_0 are given in Table 1. The flow law exponent $n = 3$. The effective strain rate $\dot{\varepsilon}_e$ is related to the second invariant of the strain rate tensor by $2\dot{\varepsilon}_e^2 = \dot{\varepsilon}_{ij}\dot{\varepsilon}_{ij}$, in which individual strain rate components are $\dot{\varepsilon}_{ij} = \frac{1}{2}\left(\frac{\partial u_i}{\partial x_j} + \frac{\partial u_j}{\partial x_i}\right)$. The deviatoric stress is $\tau_{ij} = \sigma_{ij} - \frac{1}{3}\sigma_{kk}\delta_{ij} = \sigma_{ij} + P\delta_{ij}$, where σ_{ij} is the full stress, δ_{ij} is the Krönecker delta (or identity matrix) and P is the mean compressive stress.

[10] A more general form of equation (5) is

$$\tau_{ij} = 2\eta\dot{\varepsilon}_{ij}, \tag{6}$$

where $\eta = \frac{1}{2}B(\theta)\dot{\varepsilon}_e^{\frac{1-n}{n}}$ is the temperature- and strain rate–dependent effective viscosity (variables used in formulation and solution of the energy and momentum equations are given in Table 2).

3. Orthogonal, Curvilinear Coordinate System

[11] A unique aspect of our approach is that we solve the governing equations in an orthogonal, curvilinear, boundary-fitted coordinate system. This is analogous to using polar coordinates $r = (x^2 + y^2)^{1/2}$ and $\theta = \tan^{-1}(y/x)$ to describe the location at any point on an annulus-shaped domain, where x and y are the coordinates in a standard Cartesian system. An advantage of this type of coordinate system is that there are no cross terms in the expressions for the boundary conditions, which simplifies the numerics. Details of the construction of the coordinate system for two-dimensional domains with arbitrarily shaped upper and lower boundaries are in Appendix A.

[12] Figure 1 shows an example of an orthogonal, curvilinear grid in the (x, z) domain (Figure 1a) and transformed to the $(\hat{x}, \hat{z})$ domain (Figure 1b). Length, area, and volume in the two coordinate systems are related by a set of scale factors. For an arbitrarily shaped domain, analytical expressions for the scale factors do not exist. Instead, the scale factors are calculated using the grid geometry in the (x, z) domain and the grid spacing in the $(\hat{x}, \hat{z})$ domain. For example, the unit vector $\hat{\mathbf{e}}_{\hat{x}}$ and the scale factor $h_{\hat{x}}$ along the $\hat{x}$ direction are related by

$$\hat{\mathbf{e}}_{\hat{x}} = \frac{\partial \mathbf{r}}{\partial \hat{x}}\left\|\frac{\partial \mathbf{r}}{\partial \hat{x}}\right\|^{-1} = \frac{\partial \mathbf{r}}{\partial \hat{x}}\frac{1}{h_{\hat{x}}}, \tag{7}$$

where $\mathbf{r}$ is the position vector in the (x, z) domain and $\|\mathbf{x}\|$ denotes the magnitude of the vector $\mathbf{x}$. The scale factor $h_{\hat{x}}$, which relates length in the (x, z) domain to length along the $\hat{x}$ direction, is given by

$$h_{\hat{x}} = \left\|\frac{\partial \mathbf{r}}{\partial \hat{x}}\right\| = \left[\left(\frac{\partial x}{\partial \hat{x}}\right)^2 + \left(\frac{\partial z}{\partial \hat{x}}\right)^2\right]^{\frac{1}{2}}. \tag{8}$$

Table 2. Variables Used in Heat and Momentum Balance Models

Symbol	Variable	Units
A	temperature-dependent rate factor	$\mathrm{Pa}^{-3}\ \mathrm{a}^{-1}$
$\mathbf{A}$	pentadiagonal, banded, sparse coefficient matrix	–
a_K	generic FVM coefficient at volume center K (K = P, E, W, U, D)	
α	weight factor for calculating interface diffusivities	–
B	inverse rate factor	$\mathrm{Pa\ a}^{1/3}$
$\overline{B}_{\mathrm{i}}$	volume mean body force	$\mathrm{N\ m}^{-3}$
b	generic, nonsteady, advective-diffusion equation source term	$\varphi\ \mathrm{m}^{-3}\ \mathrm{a}^{-1}$
$\dot{b}$	ice-equivalent accumulation rate at surface	$\mathrm{m\ a}^{-1}$
β	interpolation weight across time step Δt	–
D_k	diffusive mass flow rate at interface k (k = e, w, u, d)	$\mathrm{kg\ m}^{-1}\ \mathrm{a}^{-1}$
$d_P{}^u$, $d_P{}^w$	pressure and velocity correction proportionality constant	$\mathrm{m\ a}^{-1}\ \mathrm{Pa}^{-1}$
Δx_K, Δz_K	dimensions of individual volume at K (K = P, E, W, U, D)	m
δ_{ij}	Krönecker delta or identity matrix	–
δx_k, δz_k	distance between volume centers across face k (k = e, w, u, d)	m
$\dot{\varepsilon}_{ij}$	strain rate tensor	a^{-1}
$\dot{\varepsilon}_{\mathrm{e}}$	effective strain rate	a^{-1}
F_k	advective mass flow rate at interface k (k = e, w, u, d)	$\mathrm{kg\ m}^{-1}\ \mathrm{a}^{-1}$
Γ	diffusivity for generic FVM equation	–
H	ice thickness	m
J_i	combined advective and diffusive flux in direction i	flux
λ	pressure correction relaxation factor	–
n_i	Cartesian surface-normal vector	–
η	effective viscosity	Pa a
η_k	effective viscosity at volume interface k (k = e, w, u, d)	Pa a
P	pressure	Pa
P_{atm}	atmospheric pressure	Pa
P_{sfc}	surface pressure	Pa
P_k*	Estimated pressure at interface k (k = e, w, u, d)	Pa
P'_k	pressure correction at interface k (k = e, w, u, d)	Pa
Pe_k	Peclet number at interface k (k = e, w, u, d)	–
φ^{a}	scaler solution to generic FVM equation	–
S	source term for generic FVM equation	–
S_{Int}	volume-integrated source term for generic FVM equation	–
σ_{ij}	full-stress tensor	Pa
θ	absolute temperature	K
t	time	a
τ_{ij}	deviatoric stress tensor	Pa
θ_s	surface temperature	K
$\overline{u}_{\mathrm{k}}$	column-averaged velocity at finite volume face k (k = e, w, u, d)	$\mathrm{m\ a}^{-1}$
u, v	horizontal and vertical components of velocity	$\mathrm{m\ a}^{-1}$
u_K, w_K	velocity at velocity-volume centerpoint, K (K = P, E, W, U, D)	$\mathrm{m\ a}^{-1}$
u_k*, w_k*	estimated velocity at interface k (k = e, w, u, d)	$\mathrm{m\ a}^{-1}$
u'_k, w'_k	velocity correction at interface k (k = e, w, u, d)	$\mathrm{m\ a}^{-1}$
$\hat{u}_k$, $\hat{w}_k$	pseudo velocity at interface k (k = e, w, u, d)	$\mathrm{m\ a}^{-1}$
W	flow band width	m
x, z	horizontal and vertical coordinates (Cartesian)	m
$\hat{x}$, $\hat{z}$	horizontal and vertical coordinates (orthogonal, curvilinear)	–
χ	shape function for horizontal velocity	–

[a]Heat and momentum balance equations have different coefficient definitions and thus different units.

[13] The gradients enclosed in brackets are calculated numerically on the basis of the grid geometry as shown in Figure 1c. A similar expression is used to calculate the scale factor along the $\hat{z}$ direction, $h_{\hat{z}}$. Appendix A shows how the scale factors are used to scale the governing equations.

4. Boundary and Initial Conditions

[14] The energy and momentum equations are parabolic and elliptic respectively, and so either the normal gradient or the value of u, w, and θ must be specified at each boundary. Where stress is specified at a boundary, the traction vector must be continuous, and the normal and tangential gradients in u (or w) must be specified along with the pressure. The energy equation also requires specification of an initial condition for the ice temperature. For illustration, here we derive boundary conditions for the simplest orthogonal coordinate system, Cartesian coordinates, with the understanding that extension to a general, orthogonal, curvilinear coordinate system is straightforward once the appropriate scale factors are at hand. Incorporation of curvilinear geometry through scale factors is discussed in Appendix A.

[15] Continuity of the traction vector T_i across the free surface requires

$$T_i = \sigma_{ij} n_j = \left(\tau_{ij} - P\delta_{ij}\right) n_j = -P_{atm} n_i, \tag{9}$$

where P_{atm} is the atmospheric pressure and n_i are the components of the surface normal vector. Surface tension

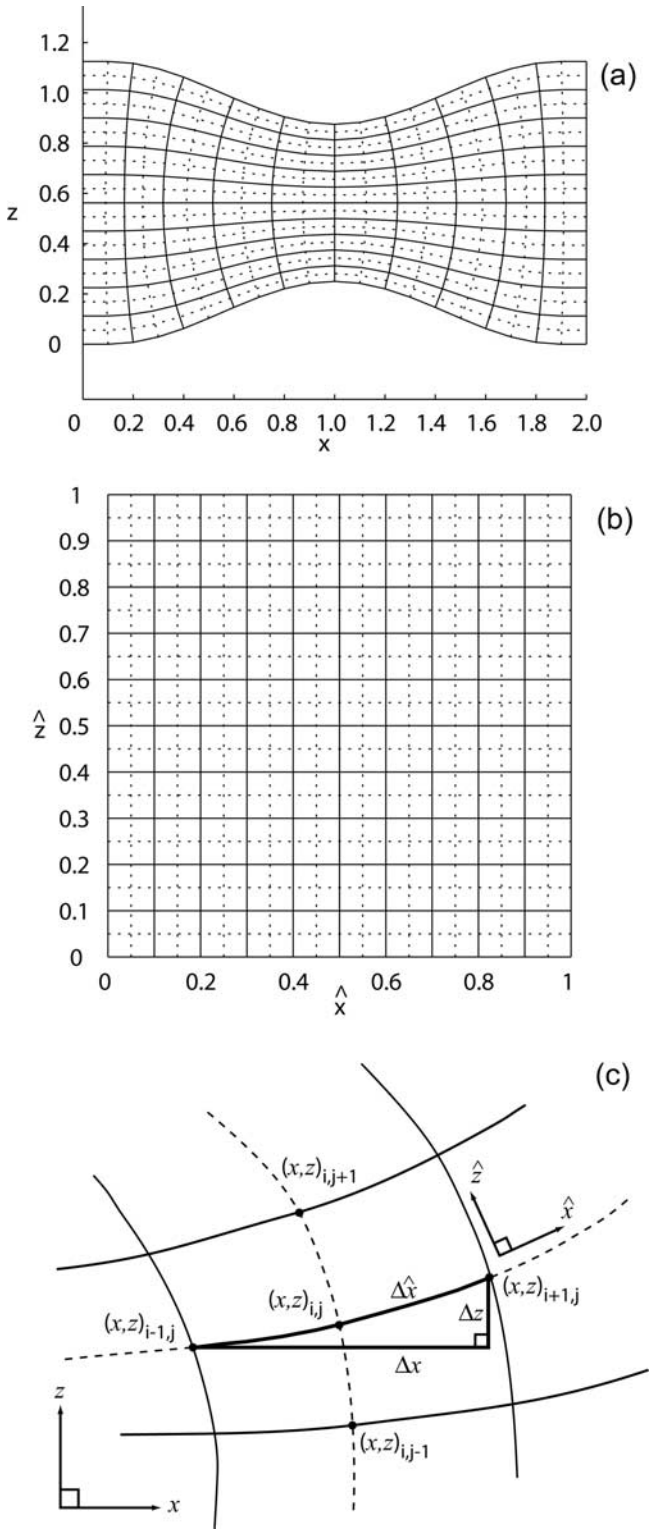

and wind stress are neglected. For a boundary-fitted coordinate system, $n_i = [0,1]^T$ on the upper surface, and so

$$\tau_{zx} = 2\eta\dot{\varepsilon}_{zx} = \eta\left(\frac{\partial u}{\partial z} + \frac{\partial w}{\partial x}\right) = 0 \tag{10}$$

$$\tau_{zz} = 2\eta\dot{\varepsilon}_{zz} = 2\eta\frac{\partial w}{\partial z} = P - P_{atm}. \tag{11}$$

[16] These describe the boundary conditions for velocity gradients that are surface-tangential $\frac{\partial u}{\partial z}\big|_{sfc} = -\frac{\partial w}{\partial x}\big|_{sfc}$ and surface-normal $\frac{\partial w}{\partial z}\big|_{sfc} = \frac{P_{sfc}-P_{atm}}{2\eta_{sfc}}$, and for the mean compressive stress at the surface $P_{sfc} = 2\eta\frac{\partial w}{\partial z}\big|_{sfc} + P_{atm}$.

[17] At the sides of the domain we specify the boundary-normal component of velocity. For example, the balance flux from a flow divide that is frozen at the bed ($u(x = 0) = w(x = 0) = 0$) to the "eastern" boundary (the right-hand side of the domain) is

$$u(z)_e = \overline{u}_e\chi(z), \tag{12}$$

where $\chi(z)$ is a shape function and the column-averaged velocity $\overline{u}_e = \frac{1}{H_e}\int_0^e \dot{b}(x)dx$, where H_e is the ice thickness at the eastern boundary ($x = e$) and $\dot{b}(x)$ is the surface accumulation rate in the x direction. Once a converged velocity solution has been found using an initial estimate for $\chi(z)$, the shape function is recalculated according to $u(z)/u_{\mathrm{sfc}}$, where $u(z)$ and u_{sfc} are taken from a velocity profile several ice thicknesses inside of the domain boundary. To minimize the influence of the boundary conditions on the solution, we specify that domain boundaries are >20 ice thicknesses beyond the region of interest.

[18] In the above example we assumed that ice is frozen at the bed, but the analysis is easily extended to include basal melting and/or sliding if the bed is at the pressure melting point. For calculating the ice temperature, the temperature gradient at the base of the underlying bedrock is specified

$$\frac{\partial\theta}{\partial z} = -\frac{Q_{geo}}{k_r}, \tag{13}$$

where Q_{geo} is the geothermal flux, and k_r is the thermal conductivity of the bedrock (generally assumed to be constant through time). The temperature at the ice surface is specified as a function of time and distance along flow,

$$\theta_s = \theta_s(x,\ t). \tag{14}$$

[19] If the ice-bed interface reaches the pressure melting point, any excess upward heat flux results in basal melting;

Figure 1. Orthogonal, curvilinear coordinate system: (a) example of $(\hat{x}, \hat{z})$ coordinate curves in (x, z) space and (b) $(\hat{x}, \hat{z})$ coordinate curves transformed into $(\hat{x}, \hat{z})$ space. In both cases, solid lines denote volume boundaries. Dashed lines intersect one another at volume centers and intersect solid lines at volume faces. Length, area, and volume in the two coordinate systems are related by a set of scale factors (equation 8)). (c) Variables needed to solve equation (8) numerically for the scale factor $h_{\hat{x}}$, which relates length in the (x, z) domain to length along the $\hat{x}$ direction.

the vertical velocity at the bed is set to the basal melt rate. Lateral domain boundaries are specified sufficiently far down flow so that the advective heat flux is orders of magnitude larger than the diffusive heat flux; at these boundaries the diffusive heat flux is set to zero. In the ice, the initial temperature field is specified using the steady state analytical solution at a flow divide [*Hooke*, 1998].

[20] We begin calculations by specifying an initial viscosity and velocity field. The initial estimate of the temperature field determines a rate factor field, from which the vertical shearing rate $\frac{\partial u}{\partial z}$ is calculated using the laminar flow approximation [*Hooke*, 1998]. The horizontal velocity field is obtained by integrating the vertical shearing rate from the bed to the surface, explicitly accounting for higher shearing rates near the bed because of warm, soft ice. The initial vertical velocity field is then estimated from continuity. An initial value for the effective viscosity is calculated using an initial estimate of the rate factor and a characteristic value for the effective strain rate ($\sim 10^{-3}$–10^{-4} a^{-1}).

5. Numerical Solution

[21] The FVM is well suited to solving ice flow problems in which horizontal stress gradients are important. Like the FDM, the FVM solves the governing equations on a structured grid. Like the FEM, the FVM solves the integral form of the governing equations, and so easily accommodates nonuniform grid spacing, providing that the grid itself is orthogonal. *Patankar* [1980] and *Versteeg and Malalasekera* [1995] give complete descriptions of the method.

[22] As discussed earlier, for simplicity we discuss solutions for rectangular domains in Cartesian coordinates. Extension to more complex curvilinear geometries is discussed in Appendix A. To avoid "checkerboard" pressure and velocity solutions, the grid is staggered: u and w calculation volumes are offset one half grid space from P and θ calculation volumes (Figure 2a). The nonsteady, advective-diffusive equation for conservation of a scalar variable φ can be written in the general form

$$\frac{\partial(\rho\varphi)}{\partial t} + u_i \frac{\partial(\rho\varphi)}{\partial x_i} = \frac{\partial}{\partial x_i}\left(\Gamma \frac{\partial \varphi}{\partial x_i}\right) + S, \tag{15}$$

where S is a source term, and Γ is the conductivity.

5.1. Conservation of Momentum

[23] An expression for the conservation of momentum in the x direction comes from substituting φ in equation (15) with the horizontal component of velocity u; Γ with the effective viscosity η; and S with the imbalance between the pressure gradient and the body force. In this case, terms on the left-hand side tend to zero because the nonsteady and advective terms are small. Integrating over the quadrilateral volume shown in Figure 2b gives

$$\eta_e \left.\frac{\partial u}{\partial x}\right|_e \Delta z_P - \eta_w \left.\frac{\partial u}{\partial x}\right|_w \Delta z_P + \eta_u \left.\frac{\partial u}{\partial z}\right|_u \Delta x_P - \eta_d \left.\frac{\partial u}{\partial z}\right|_d \Delta x_P + S_{Int} = 0. \tag{16}$$

[24] Here and below we follow a subscript convention similar to that used by *Patankar* [1980]; subscripts E, W, U, and D refer to values at volume centers adjacent to the volume centered at P and subscripts e, w, u, and d refer to values at adjacent interface centers (Figure 2b). The source term S_{Int} is the integrated imbalance between pressure gradients and the body force acting in the x direction:

$$S_{Int} = -(P_e - P_w)\Delta z_P + \overline{B}_x \Delta x_P \Delta z_P, \tag{17}$$

where $\overline{B}_x = \rho g_x$ is the mean body force acting over the calculation volume with center (x_P, z_P). P_e and P_w refer to the pressures at the east and west interfaces of the calculation volume centered at (x_P, z_P). These points are also the centers of adjacent P and θ calculation volumes (Figure 2).

[25] Equations (16) and (17) describe the balance of momentum fluxes across the east, west, upper, and lower interfaces of the volume centered at (x_P, z_P). A convenient property of an orthogonal coordinate system is that these interface fluxes are quantified by the gradient in u using piecewise-linear profiles. The gradients are calculated using values of u at the centers of the neighboring four volumes; that is, those to the east (U_E), west (U_W), above (U_U), and below (U_D). Hence the discretized form of equation (16) is

$$\eta_e\left(\frac{u_E - u_P}{\delta x_e}\right)\Delta z_P - \eta_w\left(\frac{u_P - u_W}{\delta x_w}\right)\Delta z_P + \eta_u\left(\frac{u_U - u_P}{\delta z_u}\right)\Delta x_P - \eta_d\left(\frac{u_P - u_D}{\delta z_d}\right)\Delta x_P + S_{Int} = 0. \tag{18}$$

[26] Values of δx and δz are defined in Figure 2b.

[27] The interface viscosities η_u, η_d, η_e, and η_w are analogous to the interface thermal conductivity k in the heat equation and the interface conductivity Γ in the generalized equation. The interface "conductivity" (η, k, or Γ) is often a function of the dependent variable (i.e., $\eta(u)$, $k(\theta)$, $\Gamma(\varphi)$), which is calculated at volume centers and assumed to apply over its entirety. For neighboring volumes with differing conductivities, the interface conductivity is calculated from the harmonic mean of conductivities at the adjacent volume centers [*Patankar*, 1980]. For example, the harmonic mean used to calculate η_e is

$$\eta_e = \left[\alpha \eta_E^{-1} + (1-\alpha)\eta_P^{-1}\right]^{-1}, \tag{19}$$

where $0 \le \alpha \le 1$ is a weighting factor given by $\alpha = \frac{\delta x_{e-}}{\delta x_e}$; lengths δx_{e-} and δx_e are defined in Figure 2b.

[28] From equation (18), we define the coefficients, $a_E = \frac{\eta_e \Delta z_P}{\delta x_e}$, $a_W = \frac{\eta_w \Delta z_P}{\delta x_w}$, $a_U = \frac{\eta_u \Delta x_P}{\delta z_u}$, $a_D = \frac{\eta_d \Delta x_P}{\delta z_d}$, and $a_P = a_E + a_W + a_U + a_D$, which allow us to write equation (18) as

$$a_P u_P = a_E u_E + a_W u_W + a_U u_U + a_D u_D + S_{\text{int}} \tag{20}$$

or

$$a_P u_P = \sum_{l=1}^{m} a_l u_l + S_{Int}. \tag{21}$$

[29] The subscript l denotes a "neighboring" volume (m = 4 for 2-D coordinate systems). The domain is characterized by r rows and c columns; it is described by $r \times c$ equations of the form of equation (21). To implement the boundary conditions, columns of "dummy"

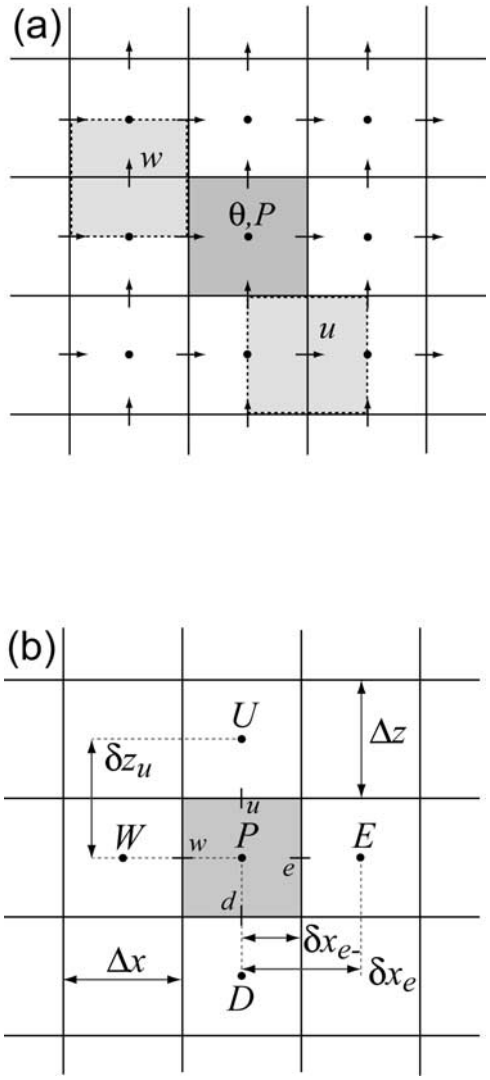

Figure 2. Staggered grid used for numerical solution of the momentum and energy balance equations. (a) Calculation volumes of u (w) offset 1/2 grid space in the horizontal (vertical) direction from θ and P calculation volumes. Velocity volume centers are θ and P interface centers and vice versa. (b) Naming convention used to define a volume centered at P with neighboring volumes centered at points to the east, west, up, and down (E, W, U, and D, respectively) and with interfaces at points e, w, u, and d. Finite volume dimensions are given by Δx and Δz. Distances δx and δz from P to the center of neighboring volumes are assigned subscripts depending on the neighboring volume (e.g., δx_e and δz_u). Distances from P to the respective interfaces are assigned an additional subscript (e.g., δx_{e-} and δz_{u-}).

volumes are added as the east and westmost columns of the coefficient arrays a_E and a_W. Similarly, rows of dummy volumes are added as the top and bottom rows of the coefficient arrays a_U and a_D. With boundary conditions included, equation (21) gives $r \times c$ linear equations in $r \times c$ unknowns:

$$\mathbf{A}\vec{u} = \vec{s}. \tag{22}$$

[30] $\mathbf{A}$ is a sparse matrix with coefficients a_E, a_W, a_U, a_D and a_P along the appropriate diagonals. $\vec{s}$ is a vector of source terms and $\vec{u}$ is the solution vector of horizontal velocity components. A similar set of equations is constructed to solve for the vertical velocity field. Because $\mathbf{A}$ is banded with nonzero elements along only five of the diagonals ($\mathbf{A}$ is "pentadiagonal"), it can be inverted directly. Any appropriate method may be used to invert the matrix; we use subroutines native to the Matlab© software package.

5.2. Conservation of Energy

[31] Conservation of energy in the x direction comes from equation (15) by substituting ϕ with $C\theta$ on the left-hand side and by substituting ϕ with θ, Γ with k, and S with heat sources due to strain heating on the right-hand side. In this case the nonsteady and advective terms cannot be neglected and the interface flux is partitioned into advective and diffusive components. Forward time stepping is handled in a fully implicit manner. Details of our treatment of the energy balance are given in Appendix B.

5.3. Calculation of the Momentum Source Term

[32] The pressure field in the momentum source term in equation (17) is not known a priori. We calculate the pressure and velocity fields using an iterative "pressure correction" method [*Patankar*, 1980; *Ferziger and Perić*, 1999; *Versteeg and Malalasekera*, 1995], which is similar to methods employed by many commercially available computational fluid dynamics packages. Briefly, an initial estimate of the pressure field (for example, hydrostatic pressure) is used to solve for the horizontal and vertical velocity fields through equation (22) and the analogous equation for the vertical component of velocity. Using these velocity solutions, the continuity equation is integrated over each volume to calculate a residual mass source (or sink); deviations from zero are used to calculate a correction to the pressure field, which is then used to solve for updated horizontal and vertical velocity fields, and to calculate an improved (smaller magnitude) estimate of the mass source within each volume. Iterations continue until the mass source is near zero. A complete description of the procedure is given in Appendix C.

5.4. Solution Procedure

[33] At each time step, the domain geometry and the boundary and initial conditions allow calculation of the velocity field, which is used as an input to calculate the energy balance and an updated temperature field. The velocity field is also used to update the domain geometry through the evolution of the free surface. The new temperature field and domain geometry are then used as inputs for calculating the velocity field for the next time step.

[34] Ice viscosity is a nonlinear function of the velocity field, which makes the momentum equations nonlinear. This nonlinearity is treated iteratively: an initial estimate of the viscosity is used to calculate the velocity field, from which updated strain rate and effective viscosity fields are calculated. Iterations continue until both the velocity and viscosity fields converge. In all tests to date, the model converges when the viscosity and pressure fields are iterated simultaneously; no subiterations are necessary.

[35] The free-surface boundary conditions discussed above require specification of values for gradients in u, w, and P at the surface, but these are not independent; for example, the boundary condition on P requires knowledge

of w and vice versa. This problem is solved by using values calculated from the previous iteration. As the viscosity, pressure, and velocity fields converge over the course of iterating, the differences between current and previous estimates of u, w, and P vanish and the boundary conditions become self-consistent.

[36] At each time step, internal heat sources are calculated from the stress and strain rate fields. We make the simplifying assumption that the dominant shear and strain rate components are σ_{zx} and $\dot{\varepsilon}_{zx}$. The temperature dependence of both $C(\theta)$ and $k(\theta)$ is small and nearly linear over the range of temperatures expected in polar ice sheets. We use the temperature field from the previous time step to calculate $C(\theta)$ and $k(\theta)$ by interpolating between known values given in Table 1. We use analytical expressions to calculate $C(\theta)$ and $k(\theta)$ in the upper firn layer [*Paterson*, 1994].

[37] Initially, the model geometry, temperature, effective viscosity, and velocity fields are far from steady state and 10^1-10^2 iterations of the momentum equations are necessary for the solutions to converge. As the model evolves toward steady state and solutions for the temperature, effective viscosity, and velocity fields converge, the number of iterations required during each time step generally decreases to $\leq 10^1$. Solutions to the momentum equations obey both integral and differential mass conservation to within machine accuracy. The number of iterations required to obtain a converged velocity solution is always greater than the single iteration needed to obtain a converged temperature solution, and so we run the energy balance model at each time step.

[38] The model domain consists of two layers: ice overlying bedrock. Momentum equations are not needed in the bedrock layer and only the heat equation (with no advection) is solved there. In order to provide adequate thermal inertia, we specify the minimum thickness of the bedrock layer to be greater than the maximum thickness of the ice at the start of a model run. The geometry and thermal properties of the bedrock layer are held constant over time. Within the ice, the velocity field and the specified accumulation rate determine changes in the shape of the domain through evolution of the free surface. For ice flow over a frozen ice-bed interface, horizontal and vertical surface velocities are $\leq 10^1$ and 10^0 m a^{-1}, respectively. In this case, updating the domain geometry at 20-year time steps is adequate to model the evolution of the surface topography. Small interpolation errors during regridding can cause small errors in volume; for example, for steady state boundary conditions (surface temperature, accumulation rate, and geothermal flux), a fractional volume change of $\sim 10^{-3}$ percent occurs when a 1×40 km domain evolves over 10^5 a. The equivalent (erroneous) rate of ice thickness change is $\sim 10^{-7}$ m a^{-1}. In applications where errors of this magnitude are unacceptable, they could be reduced by adjusting the grid spacing and/or by iterating on the momentum equations longer.

6. Model Validation

6.1. Comparison With Analytical Solutions

[39] For simple domain shapes and boundary conditions, we compare output from our model with analytical solutions:

[40] 1. *Hooke* [1998] gives a 1-D, analytical temperature solution for steady state flow at an ice divide that assumes linearly decreasing vertical velocity, no horizontal advection, and temperature-independent thermal properties. We specify these conditions in our model with constant accumulation rate and geothermal flux on a 1000 m thick rectangular slab discretized by a 100 finite volumes in the vertical direction. We approximate a steady state temperature solution by forward-time stepping 10^6a at 10^3a time steps. Our model results agree with the 1-D analytical solution to within $<10^{-3}$ K.

[41] 2. As an approximate test of a 2-D temperature solution, we compare our model with analytical solutions for steady state heat conduction within a portion of an annulus shaped domain of constant conductivity. We prescribe temperature on the outer radius, heat flux on the inner radius, and insulated domain sides. Internal heat flow is through conduction only. Our 2-D model temperature field agrees with the analytical temperature field to within 10^{-12} K. We acknowledge that this is not a rigorous test of the 2-D solution because we still only approximate a 1-D temperature field. It does, however, confirm that there is no spurious conductive heat flux within the model when we consider a highly curvilinear 2-D domain.

[42] 3. As a test of the time-dependent temperature solution, we compare the model response to a change in surface temperature with results from a 1-D (vertical), numerical, energy balance model [*Morse et al.*, 2002]. In both models we start from steady state and prescribe a -10 K step change in surface temperature, and then allow them to evolve for 2 Ma. During that period the vertical temperature profiles from the two models agree to within 0.04 K. After allowing the model to equilibrate for an additional 5 Ma under steady boundary conditions, the rate of temperature change everywhere within the domain is $\leq 10^{-12}$ K a^{-1}. We conclude that there are no spurious energy sources or sinks in our energy balance model.

[43] 4. We test our momentum-balance model using simple domain geometries and boundary conditions, and then compare these results with those from analytical solutions of the Navier-Stokes equations. Specific test cases include case a, Poiseuille flow (here we examine flow between two parallel plates); case b, isothermal flow in an inclined parallel-sided slab with Newtonian viscosity; and case c, same as case b but with a power law viscosity. In all cases we assume an infinite length in the along- and across-flow directions, in which case w is zero everywhere and u varies as a function of the vertical position only. For case a we specify no slip ($u = w = 0$) at the top and bottom boundaries, and the analytical solution for u at the sides. For cases b and c we specify a stress-free upper boundary, no slip on the bottom boundary, and the analytical solution for u at the sides. We calculate solutions on a 20×30 grid for a domain with a 1:100 aspect ratio.

[44] Gray scale plots in Figure 3 show the horizontal velocity field (normalized by the maximum velocity in each case) plotted as a function of the normalized vertical position (z/H) and the normalized distance along the domain. Figure 3 also shows for each case, the analytical solution (solid line) for the 1-D horizontal velocity field and results from our model taken from near the center of the model domain (dots). In this case, normalized horizontal velocities are expressed in percent. In all cases the velocity

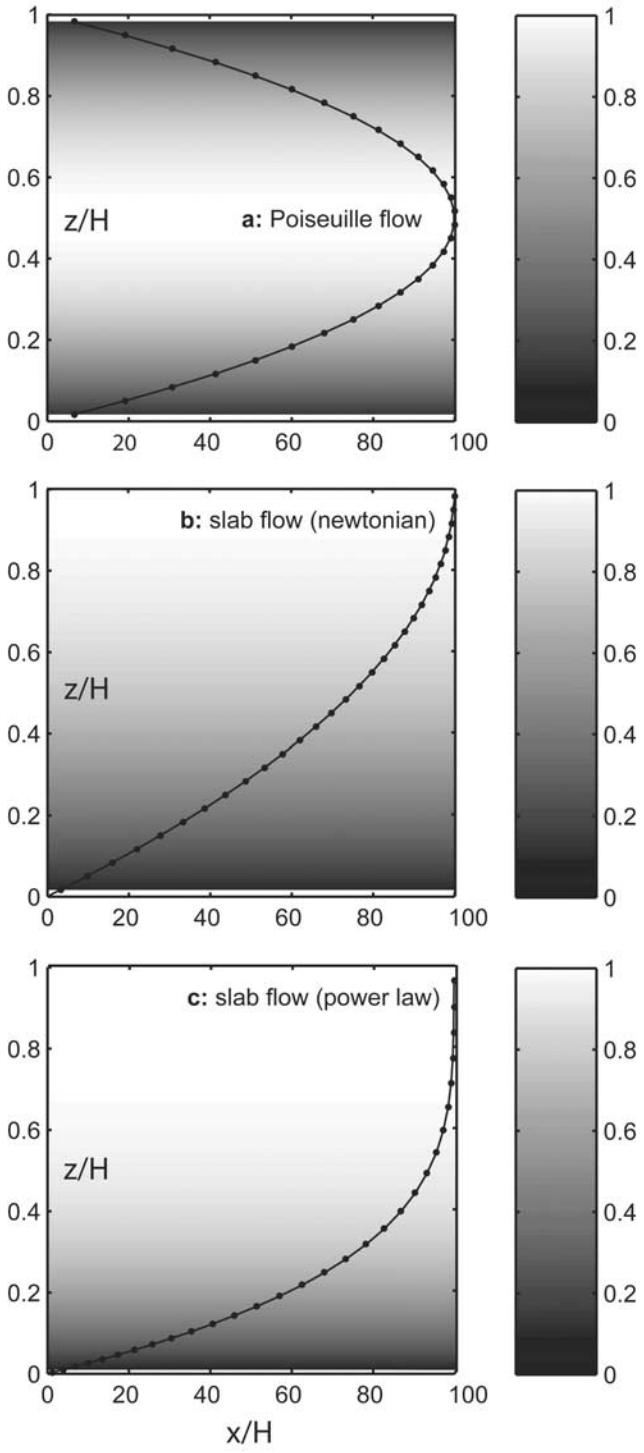

Figure 3. Numerical solutions for simple domain shapes and boundary conditions and comparison with analytical solutions. Gray scale plots show the 2-D horizontal velocity field (normalized by the maximum velocity) plotted as a function of the normalized vertical coordinate and the normalized distance along the domain for (a) Poiseuille flow; (b) isothermal, Newtonian-viscous slab flow; and (c) isothermal, power law viscous slab flow. Also shown for each case is the analytical solution (solid curve) for the normalized 1-D horizontal velocity field (expressed as percent) and results from our model near the center of the model domain (dots).

field calculated from the model is in excellent agreement with the analytical solution.

6.2. Comparison With Previous Numerical Studies

[45] Currently, there is no generally accepted set of tests for use in validating a full-stress flow model, in part because the importance of using full stress (or "higher-order") flow models has been recognized relatively recently [e.g., *Alley et al.*, 2005]. In the spirit of the European ice sheet model intercomparison study [e.g., *Huybrechts et al.*, 1996], an intercomparison of full stress and higher-order flow models is currently underway [*Pattyn et al.*, 2007]. The goal is to provide the glaciological community with a set of "benchmark" tests for validating full-stress and higher-order flow models.

[46] Although our model is a part of that intercomparison study, results are not yet available, and here we compare our model results to those from other published, full-stress numerical models. We choose two test cases for which a "correct" solution requires accounting for normal (longitudinal and vertical) stress gradients: (1) flow near an ice divide, discussed previously by *Raymond* [1983] and also by *Hvidberg* [1996], and (2) ice flow over sinusoidally varying bedrock topography, discussed previously by *Budd* [1970b] and also by *Pattyn* [2003]. Our purpose here is not to repeat the interpretation of previous authors but to demonstrate that the details of the velocity field solution from our model are consistent with those from other full stress flow models.

[47] 1. We examine flow near an ice divide for three cases: case a, isothermal flow in plane strain; case b, isothermal flow along a linearly widening flow band (modifications needed for flow bands of varying width are given in Appendix D); and case c, thermomechanically coupled flow in plane strain. In all cases the velocity fields are approximately steady state; surface temperature and accumulation are held constant and the surface shape is allowed to evolve until the rate of thickness change is $\leq 10^{-6}$ m a^{-1}.

[48] Figure 4 shows horizontal and vertical velocity shape functions from the model for these three cases. For all cases, the shape functions show the same general patterns: at and near a divide, the horizontal velocity shape functions are more linear and the vertical velocity shape functions are more parabolic in shape, relative to profiles off divide. For isothermal plane strain (Figure 4a) the width of the zone of "divide flow" (the region over which vertical velocity shape functions differ from those on the flank) is $\sim 1\times$ the ice thickness. For an isothermal flow band that widens linearly by a factor of 15 at a distance of 20 ice thicknesses (Figure 4b), the width of the zone of divide flow increases to $\sim 4\times$ the ice thickness. For the case of thermomechanically coupled flow in plane strain (Figure 4c) flow off the divide is more concentrated near the bed (where the ice is warmer and softer). For each of the three cases, our model results are in close agreement with results from full-stress, finite element models of *Raymond* [1983] and *Hvidberg* [1996].

[49] 2. We examine flow over sinusoidal bed topography for four cases in which the wavelength of the topography varies by nearly an order of magnitude. For each case, the surface topography is given by $s(x) = -x \cdot \tan(\varphi)$, where φ is a constant surface slope. The bed topography is given by $b(x) = s(x) - H + \Omega \sin\left(\frac{2\pi x}{\lambda}\right)$, where H is the ice thickness and Ω and λ are the amplitude and wavelength of the bed

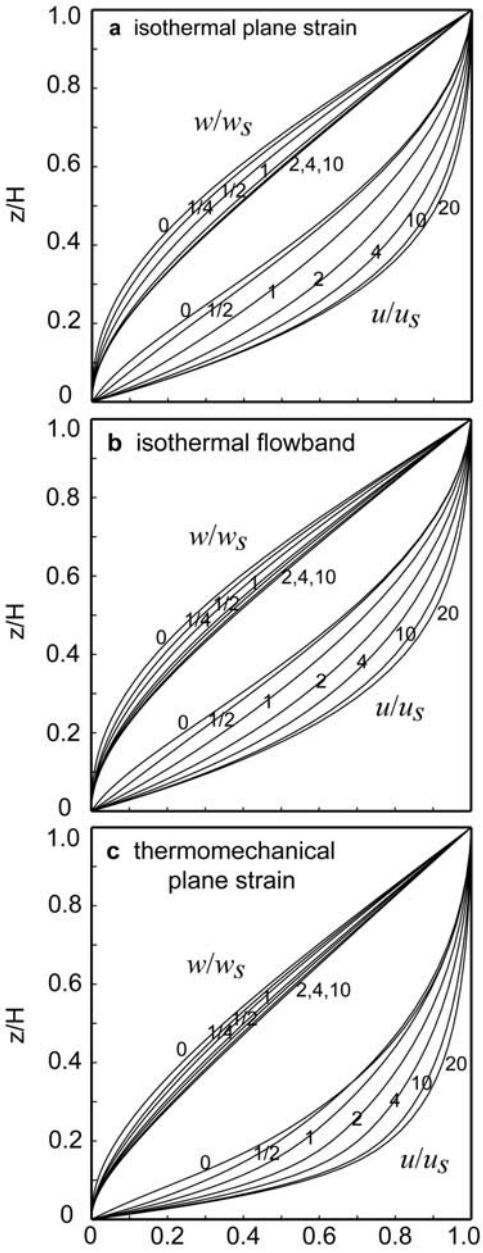

Figure 4. Modeled velocity shape functions at a flow divide. Horizontal (u/u_S) and vertical (w/w_S) velocity fields are normalized by the respective surface velocities (u_S and w_S) and are plotted as a function of the normalized vertical coordinate for (a) isothermal plane strain; (b) isothermal flow along a linearly widening flow band; and (c) thermomechanical, coupled flow in plane strain. Curves denote distance from the flow divide in units of ice thickness (0, 1/2, 1, 2, 4, 10, and 20 ice thicknesses for u and 0, 1/4, 1/2, 1, 2, 4, and 10 ice thicknesses for w).

topography, respectively. Here, $\varphi = 0.009$, $H = 1000$ m, $\Omega = H/2$, and we show results for λ of 160, 80, 40, and 20 km.

[50] Figure 5 shows horizontal (Figure 5a) and vertical (Figure 5b) surface velocities from our model (solid lines) as a function of the normalized along-flow coordinate, x/λ. Also shown (dots) are results from a full-stress, plane strain, finite element model, published by *Johnson and Staiger* [2007]. Values of relevant physical parameters are identical in both models. When λ is large, the velocity field is similar to that from a model based on the shallow-ice approximation. As λ decreases, the solution from a full-stress model demonstrates how longitudinal stress gradients smooth the velocity field spatially [e.g., *Pattyn*, 2002b, 2003]. The good agreement between the models does not mean that our model is correct, but over the range of wavelengths tested it is consistent with other full-stress models currently in use.

7. Conclusions

[51] We have developed a new, full-stress numerical ice flow model for two-dimensional domains with variable width. Our approach is similar to that used by *Hvidberg* [1996] in that we use three interacting submodels: a heat balance model, a momentum balance model, and a surface evolution model. Governing equations are solved with the FVM, which can be considered intermediate to the more commonly used FEM and FDM; it solves the integral form of the governing equations on a structured grid with nonuniform spacing and uses a FDM-like discretization scheme.

[52] A unique aspect of our model is the use of a curvilinear, orthogonal coordinate system for the description of arbitrarily shaped domains. The coordinate system has some clear advantages over structured and unstructured grids that are nonorthogonal. First, coordinate directions are everywhere parallel and perpendicular to domain boundaries, which simplifies the implementation of boundary conditions. Second, because of the orthogonal nature of the grid,

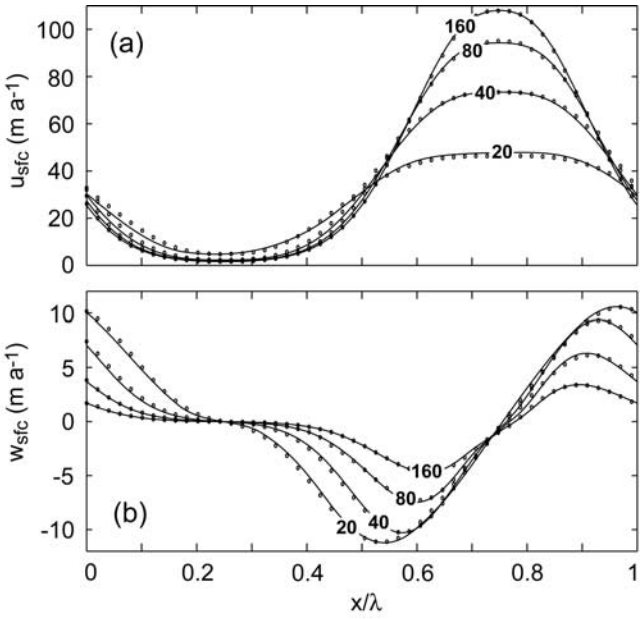

Figure 5. Flow over sinusoidal bed topography of varying wavelength λ. (a) Horizontal and (b) vertical surface velocities are plotted as a function of the normalized along-flow coordinate x/λ, from our model (curves) and from the full-stress, FEM model of *Johnson and Staiger* [2007] (dots). Numbers overlying individual curves correspond to values of λ in km. For all cases, boundary conditions include a free surface, no slip at the bed, and periodic horizontal velocities at the lateral boundaries.

Table A1. Variables Used When Creating Orthogonal, Curvilinear Coordinate System

Symbol	Variable	Units
$\mathbf{r}$	position vector Cartesian reference frame	m
$\mathbf{e}_i$	tangent vector to coordinate curve x_i	–
$\hat{\mathbf{e}}_{\hat{i}}$	unit vector along orthogonal coordinate direction $\hat{i}$	–
s	surface elevation profile in Cartesian reference frame	m
b	bed elevation profile in Cartesian reference frame	m
$\hat{z}$	stretched vertical coordinate in Cartesian reference frame and vertical coordinate in curvilinear, orthogonal reference frame	–
$\hat{x}$	horizontal coordinate in curvilinear, orthogonal reference frame	–
Δx, Δz	horizontal and vertical distance between grid points in the nonorthogonal reference frame.	m
$\Delta\hat{x}$, $\Delta\hat{z}$	horizontal and vertical distance between grid points in the orthogonal reference frame.	–
g_{ij}	surface metric for nonorthogonal reference frame	–
$\overline{g}_{ij}$	surface metric for orthogonal reference frame	–
$h_{\hat{i}}$	scale factor relating length in nonorthogonal reference frame to length along orthogonal coordinate direction $\hat{i}$	–

discretization of the governing equations leads to banded sparse matrices that can be inverted directly, rather than through iterative methods. Constructing the coordinate system is relatively straightforward and could be easily adapted for use with other solution methods that require a structured grid.

[53] While the FVM is easily extended to three dimensions, constructing a 3-D orthogonal, curvilinear coordinate system is not straightforward. For an arbitrarily shaped domain, this would require embedding the domain of interest within a larger domain with more simple boundaries, after which internal boundary conditions could be applied to the calculation domain [e.g., *Adcroft et al.*, 2004]. Computer codes are available to construct such a coordinate system; if necessary, our model could be extended to three dimensions.

[54] While some time saving is afforded by inverting the coefficient matrices directly, the iterative nature of the pressure correction method requires that numerous smaller matrices be inverted sequentially, rather than inverting for the velocity and pressure fields simultaneously in one big matrix. Run time also increases when using the model in a predictive sense, which requires regridding at each time step. Depending on the size of the time step required, regridding could take a significant amount of the total run time. On the other hand, because the continuity equation is part of the solution to the momentum equations, we need not solve an additional differential equation to describe evolution of the domain thickness. In some other full-stress and higher-order models, direct solution of the equation describing the evolution of thickness may be unstable and alternate solution methods may not conserve mass over portions of the model domain [*Pattyn*, 2003].

[55] Our model results compare very well with analytical solutions for simple domain shapes and boundary conditions. Model results also compare very well with numerical results for more complex domain shapes published by previous authors.

Appendix A: Discrete, Orthogonal, Curvilinear Coordinate System

[56] Our coordinate system, which is constructed using the method of orthogonal trajectories [*Eiseman*, 1982], requires an initial coordinate system of the form

$$\mathbf{r}(x,z) = \mathbf{r}(x, z(x,\hat{z})). \tag{A1}$$

[57] The position vector in a Cartesian reference frame $\mathbf{r}$ has components x and z, which are normalized by a convenient length scale. A ''stretched'' vertical coordinate is defined as

$$\hat{z} = \frac{z - b(x)}{s(x) - b(x)}, \tag{A2}$$

where $s(x)$ and $b(x)$ are the scaled surface and bed elevation profiles, respectively (variables used in construction of the coordinate system are given in Table A1). The $\hat{z}$ coordinate varies from 0 along $b(x)$ to 1 along $s(x)$. Rearranging equation (A2) gives

$$z(x,\hat{z}) = \hat{z} \cdot [s(x) - b(x)] + b(x). \tag{A3}$$

[58] Holding $\hat{z}$ constant and varying x produces a curve in (x, z) space; j values of constant $\hat{z}$ produces a family of j such curves. This family of $\hat{x}(x, z)$ curves constitute the set of $\hat{x}$ coordinates in the new curvilinear coordinate system shown in Figure 1a. The set of $\hat{z}$ coordinate curves perpendicular to these is derived using the method of orthogonal trajectories [*Eiseman*, 1982].

A1. Orthogonal Trajectories

[59] The method of orthogonal trajectories employs the surface metric:

$$\overline{g}_{lk} = g_{ij} \frac{\partial x_i}{\partial y_l} \frac{\partial x_j}{\partial y_k}, \tag{A4}$$

which is the rule for changing from one set of planar surface coordinates (x_1, x_2) to another (y_1, y_2). Here, $\overline{g}_{lk}$ is associated with the orthogonal, or final coordinates (y_1, y_2), and g_{ij} is associated with the nonorthogonal, or initial coordinates (x_1, x_2). Individual components of the metric tensor g_{ij} are given by the dot product of the tangent vectors:

$$g_{ij} = \mathbf{e}_i \cdot \mathbf{e}_j, \tag{A5}$$

where $\mathbf{e}_i = \frac{\partial \mathbf{r}}{\partial x_i}$ is the tangent vector in the x_i direction. An orthogonal, planar coordinate system must satisfy the condition

$$g_{12} = \mathbf{e}_1 \cdot \mathbf{e}_2 = g_{21} = \mathbf{e}_2 \cdot \mathbf{e}_1 = 0. \tag{A6}$$

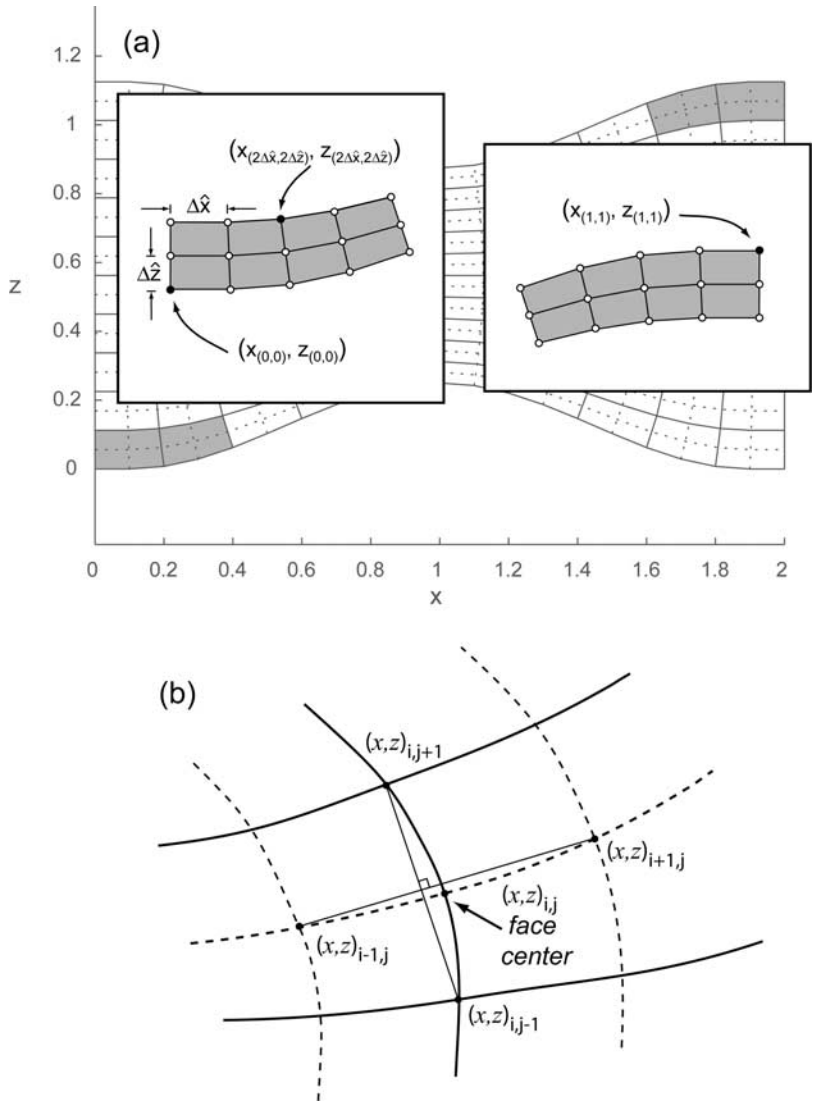

Figure A1. Discrete orthogonal, curvilinear coordinate system: (a) illustration of variables involved in the numerical integration procedure discussed in text and (b) definitions of variables when calculating discrete orthogonality at interface $(x, z)_{i,j}$. The interface at $(x, z)_{i,j}$ is shared by the finite volumes centered at the points $(x, z)_{i+1,j}$ and $(x, z)_{i-1,j}$. To obey discrete orthogonality, a line connecting these two points must be orthogonal to a line connecting the two points $(x, z)_{i,j+1}$ and $(x, z)_{i,j-1}$.

[60] Expanding equation (A4) with $(x_1, x_2) = (x, \hat{z})$ and $(y_1, y_2) = (\hat{x}, \hat{z})$ gives the "fundamental equation for orthogonal trajectories" [*Eiseman*, 1982]:

$$\frac{\partial x}{\partial \hat{z}} = \frac{-g_{12}}{g_{11}}. \tag{A7}$$

[61] It can be shown that equation (A7) can be written

$$-\frac{g_{12}}{g_{11}} = -\frac{\mathbf{e}_1 \cdot \mathbf{e}_2}{\mathbf{e}_1 \cdot \mathbf{e}_1} = -\frac{(\hat{z} \cdot (s' - b') + b')(s - b)}{1 + (\hat{z} \cdot (s' - b') + b')^2}, \tag{A8}$$

in which the primes denote derivatives with respect to x. The $\hat{z}$ coordinate curves are obtained by integrating the fundamental equation between $\hat{x}$ coordinate curves (curves of constant $\hat{z}$).

[62] Details of the numerical integration procedure are discussed later. Figure A1a shows an example in which an initial point $(x_{(0,0)}, z_{(0,0)})$ is the intersection of the lowermost domain boundary $b(x)$ along which $\hat{z} = 0$, and the leftmost domain boundary, along which $\hat{x} = 0$ (in the following discussion, subscripts refer to coordinates along the $\hat{x}$ and $\hat{z}$ coordinate curves). The goal is to find the coordinates in (x, z) space where the $\hat{z}$ coordinate curve originating at $(x_{(0,0)}, z_{(0,0)})$ intersects with the next point $(x_{(0,\Delta\hat{z})}, z_{(0,\Delta\hat{z})})$. Integrating equation (A7) from $\hat{z} = 0$ to $\Delta\hat{z}$ gives the desired x coordinate:

$$x_{(0,\Delta\hat{z})} = x_{(0,0)} + \int_0^{\Delta\hat{z}} \frac{\partial x}{\partial \hat{z}} d\hat{z}. \tag{A9}$$

[63] The corresponding z coordinate $z_{(0,\Delta\hat{z})}$ is obtained by solving equation (A3) with $x = x_{(0,\Delta\hat{z})}$ and $\hat{z} = \Delta\hat{z}$. The next

segment of the $\hat{z}$ coordinate curve is defined by starting at $x_{(0,\Delta\hat{z})}$ and integrating from $\hat{z} = \Delta\hat{z}$ to $2\Delta\hat{z}$ (for simplicity here we assume constant grid spacing in the $\hat{x}$ and $\hat{z}$ directions). The coordinate curve is complete when the last segment (that spanning $\hat{z} = 1 - \Delta\hat{z}$ and $\hat{z} = 1$) has been constructed. To build the entire grid, we continue by integrating along the $\hat{z}$ coordinate curve starting at $(x_{(\Delta\hat{x},0)}, z_{(\Delta\hat{x},0)})$, then along the curve starting at $(x_{(2\Delta\hat{x},0)}, z_{(2\Delta\hat{x},0)})$, and so on (Figure A1a). The grid is complete when the curve originating at $(x_{(1,0)}, z_{(1,0)})$ is constructed. Each grid point in $(\hat{x}, \hat{z})$ space is described by a corresponding grid point in (x, z) space. In practice, the initial coordinates, the integrand, and the integration limits in equation (A9) are row vectors and the entire suite of $\hat{z}$ coordinate curves is integrated simultaneously (discussed further below). Because the grid is discrete, rather than continuous, additional considerations are necessary to ensure orthogonality at grid point intersections.

A2. Discrete Orthogonality

[64] Maintaining the flux balance between neighboring volumes requires that the gradient in a variable at an interface must be characterized entirely by the values of the variable at the profile endpoints. With respect to a discrete grid, this is equivalent to requiring that the line segment describing the orientation of an interface be orthogonal to the line segment that connects the two volume centers that share that interface. Figure A1b illustrates discrete orthogonality at $(x, z)_{i,j}$, which denotes an interface center common to the two volumes with centers at $(x, z)_{i-1,j}$ and $(x, z)_{i+1,j}$. In the discrete sense, the grid points $(x, z)_{i,j-1}$ and $(x, z)_{i,j+1}$ define the east face of the volume centered at $(x, z)_{i-1,j}$ and the west face of the volume centered at $(x, z)_{i+1,j}$. Orthogonality at the common interface center $(x, z)_{i,j}$ requires that unit vectors paralleling the line segments defined by points $(x, z)_{i+1,j}$ and $(x, z)_{i-1,j}$, and points $(x, z)_{i,j+1}$ and $(x, z)_{i,j-1}$, have a dot product of 0. We define this condition as "discrete orthogonality". The staggered grid requires that each internal grid point obey discrete orthogonality. Individual volumes within the grid are each defined by 9 grid points: 4 corner points, 4 interface center points, and one center point. The positions of these points are constrained by orthogonality and by the locations of points defining neighboring volumes.

A3. Integration of the Fundamental Equation

[65] The $\hat{z}$ coordinate curves are obtained by integrating the fundamental equation between $\hat{x}$ coordinate curves (curves of constant $\hat{z}$). The integration scheme uses a modified Euler-predictor corrector,

$$\mathbf{x}_{j+1} = \mathbf{x}_{j-1} + \mathbf{a}\left(\hat{z}_{j+1} - \hat{z}_{j-1}\right), \tag{A10}$$

where $\mathbf{x}_{j+1}$ and $\mathbf{x}_{j-1}$ are row vectors of final and initial x coordinates, respectively, and $\mathbf{a}$ is a row vector describing the direction of travel in (x, z) space, from $\mathbf{x}_{j-1}$ to $\mathbf{x}_{j+1}$. The subscript j indicates the $\hat{x}$ coordinate curve that the set of x coordinates lie on. For example, the row vector of initial points $\mathbf{x}_{j-1}$ lies on the curve $\hat{x}_{j-1}$ (defined by $\hat{z}_{j-1} = C_{-1}$). The solution to the integration is the row vector $\mathbf{x}_{j+1}$, which has a vector of corresponding z coordinates given by

$$\mathbf{z}_{j+1} = \hat{z}_{j+1}\left[\mathbf{s}\left(\mathbf{x}_{j+1}\right) - \mathbf{b}\left(\mathbf{x}_{j+1}\right)\right] + \mathbf{b}\left(\mathbf{x}_{j+1}\right), \tag{A11}$$

which is simply the vector analog of equation (A3). Given some starting $\mathbf{x}_{j-1}$, the goal is to determine the location of $\mathbf{x}_{j+1}$ such that our definition of discrete orthogonality is obeyed at the intermediate points $\mathbf{x}_j$, $\mathbf{z}_j$. To meet this requirement, the "slope" vector $\mathbf{a}$, with components a_i, is weighted according to

$$a_i = \omega_i \left.\frac{\partial x}{\partial \hat{z}}\right|_{i,j-1} + (1 - \omega_i)\left.\frac{\partial x}{\partial \hat{z}}\right|_{i,j+1} \qquad i = 1, 2, 3, \ldots, k. \tag{A12}$$

[66] The index i indicates which of the k $\hat{z}$ coordinate curves is being integrated along; values for $\frac{\partial x}{\partial \hat{z}}$ at any index i are given by equation (A8). The weight ω_i takes on a value between 0 and 1. For $\omega_i = 1$, equation (A10) becomes a simple Euler predictor. This is the value used for "shooting" off from the lowermost domain boundary (the $\hat{x}$ coordinate curve defined by $b(x)$ and coinciding with $\hat{z} = 0$). Along this boundary the initial values for $\mathbf{x}$ are known (specified) and there is no curve $\hat{z}_{j-1} = C_{-1}$. For this initial step, j is substituted for $j + 1$ in equations (A10) and (A11). The vectors $\mathbf{x}_j$ and $\mathbf{z}_j$ obtained after this initial step define the locations of all volume centers and interface centers along the lowermost row of volumes in the grid (Figure A2a). From this set of points, the next row (Figure A2b) of points, and all rows of remaining points defining the $\hat{z}$ curves are determined as follows:

[67] 1. With all $\omega_i = 0.5$, equations (A10), (A11), and (A12) are used to predict a "trial" location for the points $\mathbf{x}_{j+1}$, $\mathbf{z}_{j+1}$.

[68] 2. A vector of discrete dot products $\mathbf{d_j}$ is calculated for the points $\mathbf{x}_j$, $\mathbf{z}_j$. For an internal grid point $(x_{i,j}, z_{i,j})$, calculation of the intersection of curves $\hat{x}_i$ and $\hat{z}_j$ is based on the line segment connecting the points (x_j, z_{j+1}) and (x_j, z_{j-1}) and the line segment connecting the points (x_{j+1}, z_j) and (x_{j-1}, z_j). The dot product for points along a domain boundary are calculated similarly but using mixed centered and one-sided differences (e.g., at the bottom boundary we calculate a centered difference in x and a forward difference in z).

[69] 3. We arbitrarily chose an orthogonality tolerance $\varepsilon = 10^{-10}$. If any point d_i within the vector $\mathbf{d_j}$ is such that $|\mathrm{d}_i| > \varepsilon$, a Newton-Raphson iteration is used to find the perturbation necessary to adjust the appropriate x_i within the $\mathbf{x}_{j+1}$ vector (and thus to also adjust the appropriate z_i in the $\mathbf{z}_{j+1}$ vector) so that $|\mathrm{d}_i| \leq \varepsilon$. Iterations of equations (A10)–(A12) continue until the points $\mathbf{x}_{j+1}$, $\mathbf{z}_{j+1}$ satisfy $|\mathbf{d_j}| \leq \varepsilon$ for the points $\mathbf{x}_j$, $\mathbf{z}_j$.

[70] 4. The calculation continues by: (1) replacing the points $\mathbf{x}_j$, $\mathbf{z}_j$ with points $\mathbf{x}_{j+1}$, $\mathbf{z}_{j+1}$; (2) replacing the points $\mathbf{x}_{j-1}$, $\mathbf{z}_{j-1}$ with points $\mathbf{x}_j$, $\mathbf{z}_j$; and (3) returning to step 1 above and predicting a new trial location for the points $\mathbf{x}_{j+1}$, $\mathbf{z}_{j+1}$.

[71] This procedure is applied to all internal grid points; no separate calculation is needed for the final row of coordinates because these are the last set of $\mathbf{x}_{j+1}$, $\mathbf{z}_{j+1}$ coordinates to be calculated (Figure A2c).

A4. Incorporation of Curvilinear Geometry Through Scale Factors

[72] Once the coordinate system has been constructed and the scale factors have been calculated, it is straightforward to adapt the governing equations and the boundary conditions to incorporate the curvilinear nature of the model

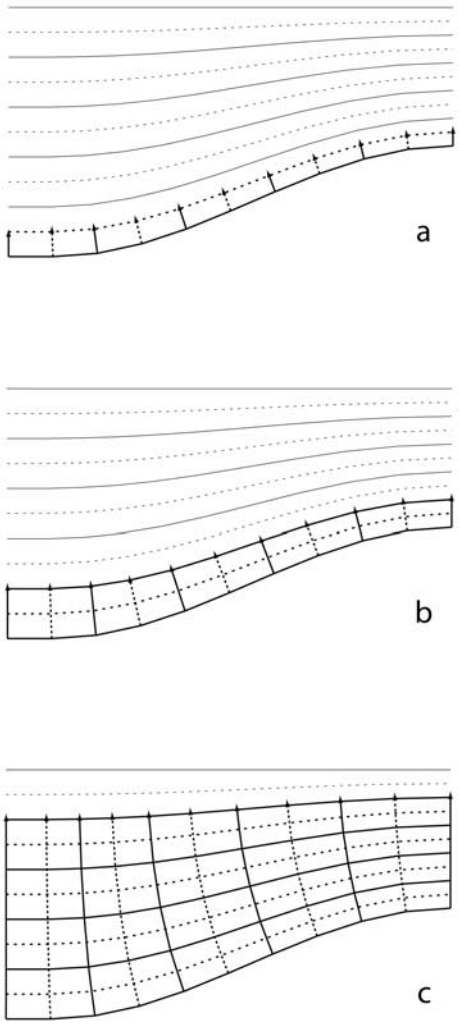

Figure A2. Section of a curvilinear grid demonstrating the integration procedure: (a) first integration, starting from the lowermost domain boundary, $b(x)$ ($\hat{z} = 0$), after which the volume centers and interface centers have been defined for the bottom row of volumes in the grid; (b) second integration, after which the upper corners and upper interface centers are defined for the bottom row of volumes in the grid; and (c) further integrations defining successively higher rows of volumes making up the grid.

domain. For example, following the rules for general, orthogonal, curvilinear coordinates [*Hughes and Gaylord*, 1964], conservation of momentum in the $\hat{x}$ direction is

$$\frac{1}{h_{\hat{x}}h_{\hat{z}}}\frac{\partial}{\partial\hat{x}}\left(\eta\frac{h_{\hat{z}}}{h_{\hat{x}}}\frac{\partial\tilde{u}}{\partial\hat{x}}\right)-\frac{1}{h_{\hat{x}}}\frac{\partial P}{\partial\hat{x}}+\rho g_{\hat{x}}=0, \tag{A13}$$

where $\tilde{u}$ is the component of velocity along the $\hat{x}$ direction (analogous to equation (2)). Similarly, the tangential, stress-free boundary condition at the free surface is

$$\frac{h_{\hat{x}}}{h_{\hat{z}}}\frac{\partial}{\partial\hat{z}}\left(\frac{\tilde{u}}{h_{\hat{x}}}\right)+\frac{h_{\hat{z}}}{h_{\hat{x}}}\frac{\partial}{\partial\hat{x}}\left(\frac{\tilde{w}}{h_{\hat{z}}}\right)=0, \tag{A14}$$

where $\tilde{w}$ is the component of velocity along the $\hat{z}$ direction (analogous to equation (10)). In equation (A14) we have applied the rules for calculating shear strain rates in general, orthogonal, curvilinear coordinates [*Hughes and Gaylord*, 1964]. In practice, scale factors are included as additional scalars in the definition of the matrix coefficients. For example the coefficient a_E defined from equation (18) becomes

$$a_E=\left(\frac{h_{\hat{z}}}{h_{\hat{x}}}\right)_e\frac{\eta_e\Delta\hat{z}}{\delta\hat{x}_e} \tag{A15}$$

and the other coefficients are altered in a similar manner. One can verify that for a Cartesian coordinate system (where the scale factors are unity) equations (A13) through (A15) revert to their familiar Cartesian counterparts.

Appendix B: Nonsteady and Advective Terms

B1. Nonsteady Term

[73] Including the nonsteady term in equation (4) requires that we also integrate over the time step, Δt. For the case of no advection ($u = w = 0$) and a flow line of unit width ($\Delta y = 1$), equation (4), becomes

$$\rho\Delta z\Delta x\left(C\theta_P^1-C\theta_P^0\right)=\int_t^{t+\Delta t}\left[k_e\left(\frac{\theta_E-\theta_P}{\delta x_e}\right)\Delta z - k_w\left(\frac{\theta_P-\theta_E}{\delta x_w}\right)\Delta z+\ldots+\overline{S}\Delta x\Delta z\right]dt, \tag{B1}$$

where superscripts indicate the value of $C\theta$ at the current time ($C\theta^0$)and at a future time ($C\theta^1$). As with the spatial discretization, an assumption is needed to describe how the dependent variables on the right-hand side of equation (B1) vary over the time step. For small time steps, it is reasonable to assume a linear variation:

$$\int_t^{t+\Delta t}\theta_P dt=\left[\beta\theta_P^1+(1-\beta)\theta_P^0\right]\Delta t, \tag{B2}$$

where $0 \le \beta \le 1$ is an interpolation weight. Similar expressions can be derived for θ_E, θ_W, θ_U and θ_D. Substituting these and the coefficients derived earlier into equation (B1) gives

$$a_P\theta_P=a_E\left[\beta\theta_E+(1-\beta)\theta_E^0\right]+a_W\left[\beta\theta_W+(1-\beta)\theta_W^0\right]+\ldots \ldots+a_U\left[\beta\theta_U+(1-\beta)\theta_U^0\right]+a_D\left[\beta\theta_D+(1-\beta)\theta_D^0\right]+b. \tag{B3}$$

[74] We drop the superscript "1" with the understanding that an unmarked variable refers to its value at the future time step. We also define several new variable definitions:

$$b\equiv\overline{S}\Delta x\Delta z+a_P^0\theta_P^0 \tag{B4}$$

$$a_P^0\equiv\frac{\rho C\Delta x\Delta z}{\Delta t} \tag{B5}$$

$$a_P\equiv a_E+a_W+a_U+a_D+a_P^0. \tag{B6}$$

[75] For $\beta = 0$, 0.5, or 1, equation (B3) reduces to one of three commonly used forms for forward-time marching when solving parabolic, partial differential equations. $\beta = 0$ results in the explicit scheme, $\beta = 0.5$ results in the semi-implicit, "Crank-Nicholson" scheme, and $\beta = 1$ results in the fully implicit scheme; here we use the fully implicit scheme.

B2. Advective-Diffusive Flux

[76] When treating the advective term in equation (4) it is convenient to first combine the advective and diffusive fluxes into a single flux term,

$$J_i = \rho u_i C\theta - k\frac{\partial \theta}{\partial x_i}. \tag{B7}$$

[77] For steady state,

$$\frac{\partial J_i}{\partial x_i} = S. \tag{B8}$$

[78] For unit width $\Delta y = 1$, integration of equation (B8) over the shaded finite volume in Figure 2b gives

$$J_e\Delta z_e - J_w\Delta z_w + J_u\Delta x_u - J_d\Delta x_d = \overline{S}\Delta x_P\Delta z_P. \tag{B9}$$

[79] For an orthogonal coordinate system, the flux across the interfaces is "one dimensional": no interface-parallel velocity components or gradients are required to quantify the interface flux. With a known flow field, the analytical expression for the advective-diffusive flux across interface e in Figure 2b is

$$J_e = F_e\left(\theta_P + \frac{\theta_P - \theta_E}{\exp(Pe_e) - 1}\right). \tag{B10}$$

[80] The Peclet number at the interface is the ratio of the advective (F_e) and the diffusive (D_e) mass fluxes across the interface: $Pe_e = \frac{F_e}{D_e} = \frac{\rho C_e u_e \Delta z_e}{k_e \delta x_e^{-1}\Delta z_e}$. Calculation of the exponential term is computationally intensive and it is convenient to use a power law approximation [*Patankar*, 1980]:

$$J_e = F_e\theta_P + [D_eA_e(|Pe_e|) + \|-F_e, 0\|](\theta_P - \theta_E), \tag{B11}$$

where $A_e(|Pe_e|) = \|0,(1 - 0.1|Pe_e|)^5\|$. Here, $\|a, b\|$ denotes that the larger of a or b is used when evaluating the enclosed expression. A_e is the area of the interface e. The advective-diffusive fluxes at interfaces w, u, and d are evaluated using similar expressions.

B3. Final Discretized Equation

[81] Including the nonsteady and advective terms in the discretized, two-dimensional equation for $C\theta$ gives

$$a_P\theta_P = a_W\theta_W + a_E\theta_E + a_D\theta_D + a_U\theta_U + b, \tag{B12}$$

where

$$a_E = D_eA_e(|Pe_e|) + \|-F_e, 0\| \tag{B13a}$$

$$a_W = D_wA_w(|Pe_w|) + \|F_w, 0\| \tag{B13b}$$

$$a_U = D_uA_u(|Pe_u|) + \|-F_u, 0\| \tag{B13c}$$

$$a_D = D_dA_d(|Pe_d|) + \|F_d, 0\|, \tag{B13d}$$

a_P and b are defined in equations (B4)–(B6). The advective and diffusive mass fluxes are

$$F_w = \rho C_w u_w \Delta z_w \tag{B14a}$$

$$F_e = \rho C_e u_e \Delta z_e \tag{B14b}$$

$$F_u = \rho C_u w_u \Delta x_u \tag{B14c}$$

$$F_d = \rho C_d w_d \Delta x_d \tag{B14d}$$

$$D_w = \frac{k_w \Delta z_w}{\delta x_w} \tag{B15a}$$

$$D_e = \frac{k_e \Delta z_e}{\delta x_e} \tag{B15b}$$

$$D_u = \frac{k_u \Delta x_u}{\delta z_u} \tag{B15c}$$

$$D_d = \frac{k_d \Delta x_d}{\delta z_d}. \tag{B15d}$$

[82] The Peclet numbers are

$$Pe_w = \frac{F_w}{D_w} \tag{B16a}$$

$$Pe_e = \frac{F_e}{D_e} \tag{B16b}$$

$$Pe_u = \frac{F_u}{D_u} \tag{B16c}$$

$$Pe_d = \frac{F_d}{D_d}. \tag{B16d}$$

Appendix C: Pressure Correction Method

[83] Following *Patankar* [1980], the pressure and velocity fields are solved iteratively using the semi-implicit method for pressure linked equations (SIMPLE) algorithm. Starting with an estimate of the pressure field P^*, the discretized velocity equations are solved to obtain estimated velocity fields u^* and w^*. A correction to the estimated pressure field P', gives corrections u' and w' to the estimated velocity fields, and updated estimates:

$$P = P^* + P' \tag{C1a}$$

$$u = u^* + u' \tag{C1b}$$

$$w = w^* + w'. \tag{C1c}$$

[84] Substituting the estimated pressures and velocities into equation (21) gives

$$a_P u_P^* = \sum_{l=1}^{m} a_l u_l^* - \left(P_e^* - P_w^*\right)\Delta z_P + \overline{B}_x \Delta z_P \Delta x_P. \tag{C2}$$

[85] Subtracting equation (C2) from equation (21) gives

$$a_P u_P' = \sum_{l=1}^{n} a_l u_l' - \left(P_e' - P_w'\right)\Delta z_P. \tag{C3}$$

[86] Here and below we use lowercase subscripts to emphasize that the pressures apply at the interfaces of the u calculation volumes. Ignoring, for the moment, the first set of terms on the RHS of equation (C3) gives

$$a_P u_P' = -\left(P_e' - P_w'\right)\Delta z_P, \tag{C4}$$

which is rearranged to

$$u_P' = -\left(P_e' - P_w'\right)\frac{\Delta z_P}{a_P} = -\left(P_e' - P_w'\right)d_P^u, \tag{C5}$$

where $d_P^u = \Delta z_P / a_P$. d_P^u is the constant of proportionality between a pressure perturbation and the corresponding perturbation to the velocity field. Substituting equation (C5) into equation (C1b) gives the corrected horizontal velocity

$$u_P = u_P^* - \left(P_e' - P_w'\right)d_P^u. \tag{C6}$$

[87] A similar expression can be derived for the corrected vertical velocity,

$$w_P = w_P^* - \left(P_u' - P_d'\right)d_P^w. \tag{C7}$$

[88] The right-hand sides of equations (C6) and (C7) describe the velocity correction at interfaces to u and w calculation volumes as a function of the bounding pressure corrections. Still needed is an expression for the pressure correction itself. The link between the pressure correction and the velocity field is the incompressibility condition. In 2-D, $\partial v/\partial y = 0$ and integration of the remaining terms in equation (3) over the shaded finite volume in Figure 2b gives

$$(u_e - u_w)\Delta z_P + (w_u - w_d)\Delta x_P = 0. \tag{C8}$$

[89] Substituting the appropriate interface velocities from equations (C6) and (C7) into equation (C8) gives

$$a_P P_P' = a_E P_E' + a_W P_W' + a_U P_U' + a_U P_U' + S. \tag{C9}$$

[90] Uppercase subscripts indicate values at the centers of pressure calculation volumes. The coefficients are $a_E = \rho d_e^u \Delta z_e$, $a_W = \rho d_w^u \Delta z_w$, $a_U = \rho d_u^w \Delta x_u$, $a_D = \rho d_d^w \Delta x_d$, $a_P = a_E + a_W + a_U + a_D$. The $r \times c$ arrays for Δx, Δz, and d at interfaces are obtained by subsampling the appropriate rows (or columns) from the larger arrays. For example, d_w^u consists of the first c columns from the array d_P^u and d_u^w consists of the last r rows of the array d_P^w; equation (C9) is solved through direct inversion of the sparse coefficient matrix.

[91] The source term in equation (C9) is the integrated continuity equation based on the velocity estimates:

$$S = \left(u_e^* \Delta z_e - u_w^* \Delta z_w\right) + \left(w_u^* \Delta x_u - w_d^* \Delta x_d\right). \tag{C10}$$

[92] A nonzero S represents a mass source (or sink) associated with each volume, and hence the degree to which the estimated velocity fields do not satisfy continuity. That is, volumes with nonzero S are associated with nonzero P', and thus nonzero u' and w' at the volume interfaces. Successive iterations of the linked pressure and velocity equations are used to generate solutions that converge toward satisfying continuity. In practice, iterations are stopped when the maximum mass residual within all of the individual volumes is less than a specified threshold.

[93] When $P'_e = P'_w$ the velocity perturbation is zero (equation (C6)). Thus, when the velocity at a boundary is specified, a zero gradient is the necessary boundary condition on P'. If the pressure at a boundary is specified, then the value of the pressure perturbation at that boundary is set to zero.

[94] The pressure correction procedure is summarized as follows:

[95] 1. Estimate a pressure field (e.g., hydrostatic pressure).

[96] 2. Use this estimate to calculate an estimated velocity field.

[97] 3. Calculate the pressure correction source term (equation (C10)).

[98] 4. Solve for the pressure correction (equation (C9)).

[99] 5. Check if the pressure correction source term is $\sim$0; If yes, the current pressure and velocity fields have converged; If no, correct the pressure and velocity fields (equations (C1a), (C6), (C7)), and return to step (3).

C1. Relaxation

[100] If the change in a dependent variable between iterations is too large, the solution may diverge or oscillate indefinitely, rather than converging. In such cases, relaxation can be used to damp the change between iterations and avoid diverging solutions. For example, a pressure perturbation can be written as

$$P' = \lambda P'_{new} + (1 - \lambda)P'_{old}, \tag{C11}$$

where the subscripts denote values calculated during the current (new) and previous (old) iterations. Changes in the pressure perturbation are underrelaxed for $0 < \lambda < 1$; they will be more gradual than without relaxation. The pressure correction method discussed above generally requires underrelaxation to both the pressure ($\lambda \sim 0.5$) and velocity perturbations ($\lambda \sim 0.8$). Further discussion on the implementation of relaxation is given by *Patankar* [1980].

C2. Alternate, Improved Solution Method

[101] The pressure correction method described above ignores the fact that the velocity correction in any volume depends not only on the pressure correction in neighboring volumes, but also on the velocity corrections in neighboring

volumes (hence the "semi-implicit" in SIMPLE). This omission is allowable because the method leads to a set of pressure and velocity fields that satisfy continuity, but it does have shortcomings. Because the velocity field is corrected by changing the pressure field alone, pressure corrections can be large and the solution may not converge. The usual remedy is to invoke underrelaxation to changes in the pressure field, but this can slow convergence.

[102] The SIMPLE-Revised (SIMPLER) algorithm [*Patankar*, 1980] addresses this shortcoming. Rearranging equation (21) gives

$$u_P = \frac{\sum_{l=1}^{n} a_l u_l + \overline{B}_x \Delta x_P \Delta z_P}{a_P} - \frac{(P_e - P_w)\Delta z_P}{a_P}. \tag{C12}$$

[103] If we define $\hat{u}_P = \frac{\sum_{l=1}^{n} a_l u_l + \overline{B}_x \Delta x_P \Delta z_P}{a_P}$, then equation (C12) becomes

$$u_P = \hat{u}_P - (P_e - P_w) d_P^u. \tag{C13}$$

[104] The first term on the RHS is the "pseudovelocity" (the velocity that would exist in the absence of the pressure field). The coefficient d_P^u is the same as defined above in equation (C5). Equation (C13) and its counterpart for the vertical component of velocity have the same form as equations (C6) and (C7) above. Inserting these expressions into equation (C8) gives

$$a_P P_P = a_E P_E + a_W P_W + a_U P_U + a_U P_U + S. \tag{C14}$$

[105] The source term is

$$S = (\hat{u}_e \Delta z_e - \hat{u}_w \Delta z_w) + (\hat{w}_u \Delta x_u - \hat{w}_d \Delta x_d), \tag{C15}$$

which is the integrated continuity equation based on the interface pseudovelocities.

[106] Unlike SIMPLE, where the initial pressure field is estimated, SIMPLER calculates the initial pressure field from equation (C1), which requires an initial estimate for the pseudovelocity fields in equation (C15). After calculating the pressure field, SIMPLER proceeds in a manner similar to SIMPLE: (1) u and w fields are calculated; (2) P', u' and w' are calculated; (3) the velocity field is corrected via $u'(P')$ and $w'(P')$. Unlike SIMPLE, the pressure field is not corrected. Rather, the corrected velocity field gives updated pseudovelocities and an updated pressure field for the next iteration. Because the pressure field is not corrected with P', the pressure corrections do not require underrelaxation ($\lambda = 1$) and the velocity corrections require only minor relaxation ($\lambda \sim 0.95$). Computation time using SIMPLER is typically 30–50% less than when using SIMPLE [*Versteeg and Malalasekera*, 1995]; we use SIMPLER when solving the momentum equations.

[107] For geometries, pressures, viscosities, and velocities relevant to a polar ice sheet, we found that SIMPLER does not consistently converge to an arbitrarily chosen degree of accuracy. We suspect that this occurs because of large round-off errors, which arise because the magnitude of the pressure field is many orders of magnitude larger than the other fields. We overcome this problem by nondimensionalizing the momentum equations in the manner described by *Raymond* [1983].

Appendix D: Flow Band Adaptation

[108] Several modifications are made to adapt the "flow line" model (where momentum and continuity are invariant in the across-flow direction) to a "flow band" model that allows for the effects of converging or diverging flow. For a flow band with width $W(x)$ varying in the along-flow direction, the across-flow gradient in velocity is [*Waddington*, 1981]

$$\frac{\partial}{\partial y} v(x,z) = \dot{\varepsilon}_{yy} = \frac{u(x,z)}{W(x)} \frac{\partial}{\partial x} W(x), \tag{D1}$$

where v is the across-flow component of velocity, and $\dot{\varepsilon}_{yy}$ is its across-flow gradient. Of interest here are the effects of lateral convergence or divergence on the horizontal and vertical velocities and the effects of $\dot{\varepsilon}_{yy}$ on the ice viscosity. For flow bands of varying width, we use the strain rate $\dot{\varepsilon}_{yy}$ from equation (D1) in equation (6). For flow bands of constant width, $\dot{\varepsilon}_{yy} = 0$ and the flow band and flow line formulations are identical.

[109] Several other minor adjustments are necessary for flow bands of varying width. First, the coefficients defined from equation (18) must be scaled by the width of the individual finite volume. For example, the coefficient a_E becomes

$$a_E = \frac{\eta_e \Delta z}{\delta x_e} W_e, \tag{D2}$$

where W_e is the width at the east face of the shaded volume centered at P in Figure 2b. Similar adjustments are made to the other coefficients associated with equation (C9). Second, the estimated velocities on the RHS of equation (C10) must also be scaled by their respective interface widths; for a flow band equation (C10) becomes

$$S = \left(\left[u^* W \Delta z \right]_e - \left[u^* W \Delta z \right]_w \right) + \left(\left[w^* W \Delta x \right]_u - \left[w^* W \Delta x \right]_d \right), \tag{D3}$$

where subscripts indicate that all values enclosed by brackets apply at their respective interfaces. Similar modifications are needed when using SIMPLER. Lastly, the specified flux boundary condition must be altered so that the surface accumulation rate is integrated over both the length and width of the flow band. In this case, the column-averaged velocity at the eastern boundary is

$$\overline{u}_e = \frac{1}{H_e W_e} \int_{x=0}^{x=e} \dot{b}(x)\, W(x) dx, \tag{D4}$$

where W_e is the width at the eastern boundary.

[110] **Acknowledgments.** We thank Charlie Raymond, Bob Bindschadler, and Tom Neumann for helpful comments on early drafts of this paper. We thank Jesse Johnson for his insight and suggestions throughout this work and also for providing results from his flow model. We also thank the editors and two anonymous reviewers for insightful comments that improved the manuscript. This work was supported by NSF grants OPP-0125610 and OPP-0087345.

References

Adcroft, A., J. Campin, C. Hill, and J. Marshall (2004), Implementation of an atmosphere-ocean general circulation model on the expanded spherical cube, *Mon. Weather Rev.*, *132*(12), 2845–2863.

Alley, R., P. Clark, P. Huybrechts, and I. Joughin (2005), Ice-sheet and sea-level changes, *Science*, *310*, 456–460.

Budd, W. (1970a), The longitudinal stress and strain-rate gradients in ice masses, *J. Glaciol.*, *9*, 19–27.

Budd, W. (1970b), Ice flow over bedrock perturbations, *J. Glaciol.*, *9*, 29–48.

Engelhardt, H. (2004), Ice temperature and high geothermal flux at Siple Dome, West Antarctica, from borehole measurements, *J. Glaciol.*, *50*, 251–256.

Eiseman, P. (1982), Orthogonal grid generation, in *Numerical Grid Generation*, edited by J. Thompson, pp. 193–233, Elsevier Sci., New York.

Ferziger, J., and M. Perić (1999), *Computational Methods for Fluid Dynamics*, Springer, London.

Fowler, A., and D. Larson (1978), On the flow of polythermal glaciers I. Model and preliminary analysis, *Proc. R. Soc. London, Ser. A*, *363*, 217–242.

Hooke, R. (1998), *Principles of Glacier Mechanics*, Prentice-Hall, Upper Saddle River, N. J.

Hughes, W., and E. Gaylord (1964), *Basic Equations of Engineering Science*, Schaum, New York.

Hutter, K. (1981), The effect of longitudinal stress on the shear stress of an ice sheet: In defense of using stretched co-ordinates, *J. Glaciol.*, *27*, 39–56.

Huybrechts, P., A. Payne, and the EISMINT Intercomparison Group (1996), The EISMINT benchmarks for testing ice-sheet models, *Ann. Glaciol.*, *23*, 1–12.

Hvidberg, C. (1996), Steady-state thermomechanical modeling of ice flow near the centre of large ice sheets with the finite-element method, *Ann. Glaciol.*, *23*, 116–123.

Johnson, J. V., and J. W. Staiger (2007), Modeling long-term stability of the Ferrar Glacier, East Antarctica: Implications for interpreting cosmogenic nuclide inheritance, *J. Geophys. Res.*, *112*, F03S30, doi:10.1029/2006JF000599.

Morse, D., D. Blankenship, E. Waddington, and T. Neumann (2002), A site for deep ice coring in West Antarctica: Results from aerogeophysical surveys and thermo-kinematic modeling, *Ann. Glaciol.*, *35*, 36–44.

Nye, J. (1957), The distribution of stress and velocity in glaciers and ice sheets, *Proc. R. Soc. London, Ser. A*, *239*, 113–133.

Patankar, S. (1980), *Numerical Heat Transfer and Fluid Flow*, Hemisphere, New York.

Paterson, W. (1994), *The Physics of Glaciers*, Elsevier Science, Oxford, U. K.

Pattyn, F. (2002a), Transient glacier response with a higher-order numerical ice-flow model, *J. Glaciol.*, *48*, 467–477.

Pattyn, F. (2002b), Ice-flow characteristics over a rough bedrock: Implications for ice-core interpretation, *Polar Meteorol. Glaciol.*, *16*, 42–52.

Pattyn, F. (2003), A new three-dimensional higher-order thermomechanical ice sheet model: Basic sensitivity, ice stream development, and ice flow across subglacial lakes, *J. Geophys. Res.*, *108*(B8), 2382, doi:10.1029/2002JB002329.

Pattyn, F., and ISMIP-HOM participants (2007), ISMIP-HOM: Results of the higher-order ice sheet model intercomparison exercise, *Geophys. Res. Abstr.*, *9*, 01351.

Price, S., and J. Walder (2007), Modeling the dynamic response of a crater glacier to lava-dome emplacement: Mount St. Helens, Washington, U.S.A., *Ann. Glaciol.*, *45*, 21–28.

Price, S., R. Bindschadler, C. Hulbe, and D. Blankenship (2002), Force balance along an inland tributary and onset to Ice Stream D, West Antarctica, *J. Glaciol.*, *48*, 20–30.

Price, S., H. Conway, E. Waddington, and R. Bindschadler (2005), Investigating feedbacks between basal sliding, frictional melting, and longitudinal-stress transmission, *Eos Trans. AGU*, *86*(52), Fall Meet. Suppl., Abstract C44A-06.

Price, S. F., H. Conway, and E. D. Waddington (2007), Evidence for late Pleistocene thinning of Siple Dome, West Antarctica, *J. Geophys. Res.*, *112*, F03021, doi:10.1029/2006JF000725.

Raymond, C. (1983), Deformation in the vicinity of divides, *J. Glaciol.*, *34*, 357–373.

Versteeg, H., and W. Malalasekera (1995), *An Introduction to Computational Fluid Mechanics: The Finite Volume Method*, Pearson Educ., Essex, U. K.

Waddington, E. (1981), Accurate modeling of glacier flow, Ph.D. dissertation, Univ. of B. C., Vancouver, B. C., Canada.

Whillans, I., and S. Johnsen (1983), Longitudinal variations in glacial flow: Theory and test using data from the Byrd Station Strain Network, Antarctica, *J. Glaciol.*, *29*, 78–97.

H. Conway and E. D. Waddington, Department of Earth and Space Sciences, University of Washington, Seattle, WA 98195, USA.

S. F. Price, Bristol Glaciology Centre, School of Geographical Sciences, University of Bristol, Bristol BS8 1SS, UK. (s.f.price@bristol.ac.uk)